

# Semi-supervised, Topology-Aware Segmentation of Tubular Structures from Live Imaging 3D Microscopy

Kasra Arnavaz	kasra@di.ku.dk
Department of Computer Science, University of Copenhagen, Denmark	
Oswin Krause	oswin.krause@di.ku.dk
Department of Computer Science, University of Copenhagen, Denmark	
Jelena M. Krivokapic	jelena.krivokapic@sund.ku.dk
DanStem, University of Copenhagen, Denmark	
Silja Heilmann	silja.heilmann@sund.ku.dk
DanStem, University of Copenhagen, Denmark	
Jakob Andreas Bærentzen	janba@dtu.dk
DTU Compute, Denmark	
Pia Nyeng	pnyeng@ruc.dk
Department of Science and Environment, RUC, Denmark	
Aasa Feragen	afhar@dtu.dk
DTU Compute, Denmark	

## Abstract

Motivated by a challenging tubular network segmentation task, this paper tackles two commonly encountered problems in biomedical imaging: Topological consistency of the segmentation, and limited annotations. We propose a topological score which measures both topological and geometric consistency between the predicted and ground truth segmentations, applied for model selection and validation. We apply our topological score in three scenarios: i. a U-net ii. a U-net pretrained on an autoencoder, and iii. a semisupervised U-net architecture, which offers a straightforward approach to jointly training the network both as an autoencoder and a segmentation algorithm. This allows us to utilize un-annotated data for training a representation that generalizes across test data variability, in spite of our annotated training data having very limited variation. Our contributions are validated on a challenging segmentation task, locating tubular structures in the fetal pancreas from noisy live imaging confocal microscopy.

**Keywords:** semi-supervised, segmentation, tubular, topology, confocal microscopy

## 1. Introduction

Segmentation of tubular structures is a common task in medical imaging, including blood vessels Zhang et al. (2019), airways Qin et al. (2019), ductal systems Wang et al. (2020b), neurons Li et al. (2019) and more. This is usually a step towards analysing the topological network structure of the organ, and it is therefore crucial that the segmented network structure is reliable. In practice, segmentation algorithms are trained to optimize voxel-based measures such as cross-entropy or accuracy. This, however, does not take into account how a small segmentation error viewed from the pixel point of view might, in fact, lead to a crucial error in the segmented network, see Fig. 1 (left).

This has motivated previous work defining segmentation loss functions that encourage topologically consistent segmentations via persistent homology Hu et al. (2019); Wang et al. (2020a). Such losses compare the numbers of components and loops between ground truth and segmentation throughout a parameterized “filtration”. While promising, this approach suffers from two problems: First, its high computational burden limits application in typical biomedical segmentation problems: current versions apply to 2D images, where they are forced to resort to enforcing topological consistency of small patches rather than globally. Second, computational topology tends to focus on topological equivalence of structure without taking its *geometry* into account. More precisely, numbers of components and loops are compared between prediction and ground truth without considering whether they actually *match*. This is suboptimal if two patches contain non-matching components or loops.

Rather than a topological loss function used during training, we propose a topological score which can be used to tune hyper-parameters on a validation set. This topological score measures topological preservation of predictions compared to annotations. Topology is represented by network skeletons, whose components and loops are soft matched based on geometry. Finally, the topological score is defined based on their agreement.

This paper aims to solve a tubular segmentation task from bioimaging. During embryonic development, the tubular network in the pancreas remodels from a web-like network to a tree-like structure Pan and Wright (2011); Villasenor et al. (2010). The pancreas is a tubular organ that produces hormones and enzymes. It has been suggested that emergence of the hormone producing cells depend on the reorganization of the tubular structure Kesavan et al. (2009); Bankaitis et al. (2015). A quantitative verification of this hypothesis requires topological accurate detection of the pancreatic tubes from noisy live imaging confocal 3D microscopy. This paper tackles segmentation of a dataset from a research project, which collected time-lapse 3D images from mouse pancreatic organs as they underwent the process of tubular re-organization and emergence of hormone producing cells.

## 2. Methods

### 2.1 Topological score function

The topology of a segmented tubular structure is represented via its skeleton Bærentzen and Rotenberg (2020); Bærentzen and et al. (2020). Our topological score is defined via the following steps: i) matching skeletal nodes; ii) soft-matching components and loops using a point cloud Intersection-over-Union (IoU) score, and iii) collecting these into a topological score.

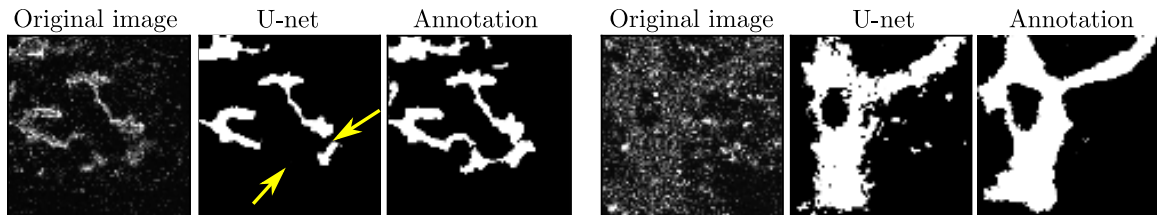


Figure 1: 2D slices. **Left:** Small voxel error, large network error. **Right:** Effect of noise.

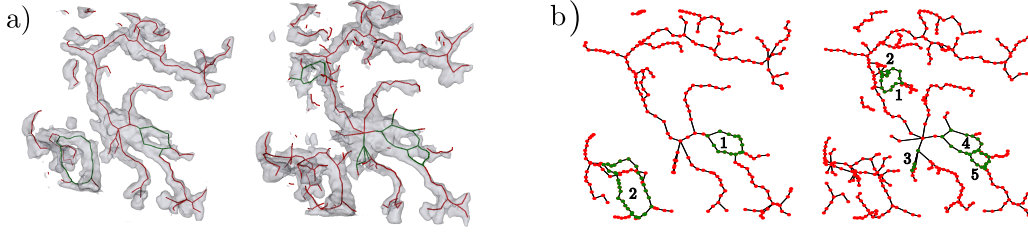


Figure 2: a) Ground truth (left) and predicted (right) segmentations (a) and their skeletons. b) 2D projections of the skeletons. Green nodes take part in loops. Note that the ground truth segmentation has 2 loops and 7 components, while the prediction has 5 loops and 10 components, of which one overlaps with the ground truth.

**i) Matching individual nodes.** Given binary ground truth- and predicted segmentations, we denote their skeleton graphs by  $S_{gt}$  and  $S_p$ , respectively. Due to noise, predicted segmentations are bumpier than the ground truth, giving higher node density in skeletons, and the topological score needs to be robust to this. We therefore match skeletal components and loops by first matching their nodes as follows (see also Fig. 3). For every component in one of the skeletons  $S_*$ , each node is matched to its nearest node in a component from the *other* skeleton  $S_*$  if such a node exists within a fixed radius  $r > 0$ ; otherwise the node is considered unmatched. Matching several nodes in one skeleton to the same node in the other skeleton is allowed. The same matching procedure is applied to loops.

**ii) Soft matching of loops and components via Point Cloud IoU.** Next, we define a strategy for partial matching of components and loops. With skeleton nodes matched, some components or loops may overlap partly, as shown in Fig 3. We need to measure this, again being robust to differences in skeleton node density.

Define  $TP_p$  to be the number of nodes in the predicted loop that is matched to a point in the ground truth (GT) loop;  $TP_{gt}$  the number of nodes in the GT loop that is matched to a point in the predicted loop,  $FP$  the number of nodes in the predicted loop that is not matched to a point in the GT loop, and  $FN$  the number of loops in the GT loop that is not matched to a point in the predicted loop. Similarly for components. Now, we might naïvely define the IoU score as

$$\frac{TP_{gt} + TP_p}{TP_{gt} + TP_p + 2FP + 2FN}.$$

However, this is not robust to different node density. Instead, in analogy with samples from probability distributions, we define the point cloud IoU:

$$\text{IoU} = \frac{\frac{TP_{gt}}{TP_{gt} + FN} + \frac{TP_p}{TP_p + FP}}{\frac{TP_{gt} + 2FN}{TP_{gt} + FN} + \frac{TP_p + 2FP}{TP_p + FP}}. \quad (1)$$

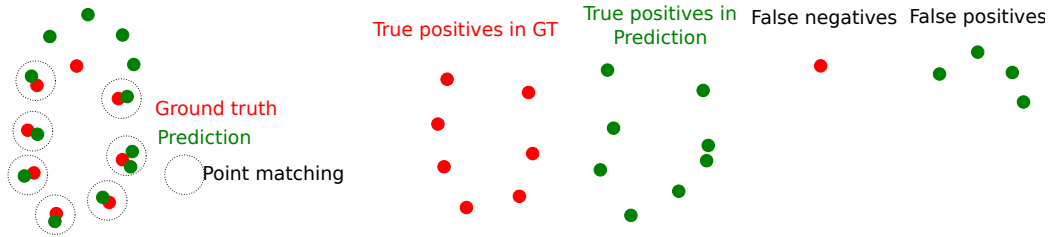


Figure 3: An example of point matching for two loops (edges not drawn).

**iii) A topological score for comparison of segmentations.** Given skeletons  $S_{gt}$  and  $S_p$ , we define two topological scoring matrices; one for components and one for loops. As in the example of Fig. 4, the loop score matrix has size  $L_{gt} \times L_p$ , where  $L_{gt}$  and  $L_p$  is the number of loops in  $S_{gt}$  and  $S_p$ , respectively. For each pair of GT and prediction loops, their matrix entry is given by their point cloud IoU of Eq. (1). Any IoU below a threshold  $t_{low}$  is set to 0, indicating no match, and any IoU over  $t_{high}$  is set to 1, indicating perfect match.

By adding along columns we obtain a per-loop column score indicating the degree to which a ground truth loop is found. Similarly, summing over rows, the row score indicates the level of correctness per predicted loop. These row and column scores can, in principle, add up to more than one when nodes appear in multiple loops; they are clipped to be at most 1. The mean row score is an analogy of recall, rewarding fewer false negatives; the mean column score is an analogy of precision, rewarding fewer false positives; and the mean of the two mean scores is an analogy of the F1 score; we refer to this as the loop score. A component score is defined analogously; the final topology score is given by the mean of the loop and component scores.

The above does not handle cases where either the GT or prediction has no loops (or components). If neither skeleton has loops, the loop score is 1. If  $S_{gt}$  has no loops, then the loop score is  $1/(1 + \#err)$ , where  $\#err$  is the number of loops found in  $S_p$ . If the  $S_p$  has no loops, then the final score is  $1/(1 + \#err)$ , where  $\#err$  is the number of loops found in  $S_{gt}$ . Components are handled similarly.

## 2.2 Semisupervised U-net architecture

Our application offers abundant unlabeled data and a small labeled subset of limited variation – a very common situation in biomedical imaging. By learning features also from

Diagram illustrating the calculation of a loop score using a 2x5 matrix. The matrix is thresholded to a 2x5 binary matrix. Row and column scores are then calculated, and the loop score is the average of these two scores.

Figure 4: Example computation of the loop score for the prediction shown in Fig. 2. The ground truth segmentation has 2 loops while the prediction has 5. Here, loop 1 in  $S_{gt}$  has overlap with loops 4 and 5 in  $S_p$ , where the first is thresholded as a perfect match and the second is thresholded as no match.

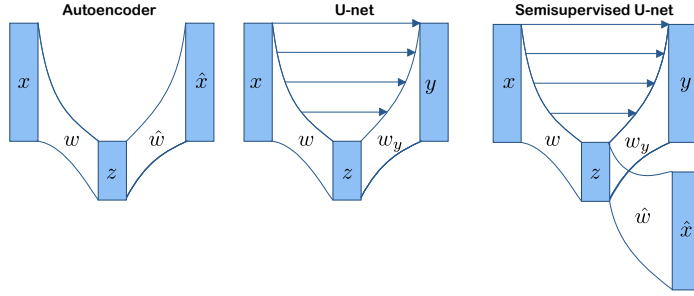


Figure 5: Semi-supervised U-net combines an autoencoder (left) with a U-net (middle) into a combined network (right) which is simultaneously trained for segmentation and reconstruction, allowing us to learn features on a large, unlabeled dataset with rich variation. A detailed description of the networks, along with training losses and reconstruction images can be found in the supplementary material.

the unlabeled data, the increased diversity obtained by including unlabeled images might improve generalization to the full distribution of data expected at test time. To this end, we use a semisupervised U-net architecture combining an autoencoder with a U-net, as shown in Fig. 5 (right).

The loss function for the semisupervised U-net is the weighted combination  $L = \alpha L_R + \beta L_S$  of the reconstruction loss  $L_R$  and the segmentation loss  $L_S$  where  $\alpha$  and  $\beta$  are hyperparameters. In our experiments,  $L_R$  is the mean squared error, and  $L_S$  is binary cross-entropy. The segmentation loss is set to zero for unlabeled images. Although the segmentation decoder  $w_y$  is trained only on the labeled images, it is implicitly affected by the unlabeled data via its dependence on the encoder  $w$  which, along with  $\hat{w}$ , is trained on both labeled and unlabeled images.

We benchmark the semi-supervised U-net against i) a U-net initialized randomly and trained solely on labeled images, and ii) against a U-net trained on labeled images, whose encoding weights  $w$  are initialized at the optima of an autoencoder trained on both labeled and unlabeled images. What separates the semisupervised U-net architecture from the U-net pre-trained on an autoencoder is the joint optimization of the two losses. We believe—as backed up by our experiments—that this joint optimization tailors the representations we learn from the unlabeled images to suit the segmentation task, and help them generalize to more diverse images than those annotated for training.

### 3. Data and preprocessing

The data used in this paper is extracted from 3D images obtained by live imaging of embryonic mouse pancreas (E12.5) explants every 10 minutes for 48 hours using a Zeiss LSM780 confocal microscope equipped for live imaging. The data is noisy and challenging, and is partially annotated by a trained expert. Their resolution is  $1024 \times 1024 \times D$ , where  $D$  varies between 27 and 40. Each image is divided into a  $4 \times 4$  grid of patches in the  $x$ - $y$  plane, each of size  $256 \times 256 \times D$ .

Table 1: Segmentation performance assessed via standard IoU as well as the topological score (Sec. 2.1). Model selection was done using both standard IoU (left) and the topological score (right) to select the shown optimal thresholds (Thr).

Architecture	Voxel-tuned			Topo-tuned		
	Thr	Voxel IoU	Topo-Score	Thr	Voxel IoU	Topo-Score
U-net	0.8	0.474±0.208	0.385±0.256	0.9	0.449±0.214	0.423±0.269
AE+U-net	0.6	0.447±0.207	0.378±0.257	0.7	0.418±0.214	0.369±0.222
Semisupervised	0.7	<b>0.490±0.226</b>	<b>0.433±0.254</b>	0.7	<b>0.490±0.226</b>	<b>0.433±0.254</b>

The mean intensity is close to zero, as the foreground volume is relatively small. The intensity variance, however, differs considerably, and there are imaging artifacts in the form of clusters of very bright pixels in some images.. As preprocessing, every image is standardized to have zero mean and standard deviation 1, and image intensities are clipped to take values within 3 standard deviations.

All our models are trained on image patches. To avoid artifacts and degradation of performance near patch boundaries, we pad the image patches with a 32 pixel wide border, making boundary effects negligible. We thus use  $320 \times 320$  patches, extracting predictions for the inner  $256 \times 256$  region.

Our labeled training set consists of patches drawn from 6 manually segmented full 3D images from 3 different movies. The training set for the autoencoder and semisupervised U-net further includes patches from 20 un-annotated images from 10 movies. Our validation- and test sets consist of 28 and 68 manually segmented 3D image patches, respectively. Here, patches were annotated in place of full images to obtain maximal data variation. Each test set patch was also given a labeling difficulty score, from 0 = easy to 3 = difficult.

## 4. Experiments and results

We compare the semisupervised U-net to a standard U-net, as well as a U-net whose encoder branch has been pretrained as an autoencoder as described in Sec. 2.2. Each architecture is optimized using Adam Optimizer with learning rate  $10^{-5}$ ,  $\beta_1 = 0.9$ , and  $\beta_2 = 0.999$ . Random weight initializations are done by Xavier uniform initializer, and biases are set to zero initially. The U-net was trained for 200 epochs, the autoencoder in AE+U-net was trained for 20 epochs which resulted in satisfactory reconstructions and the U-net part was trained for 200 epochs. For the semi-supervised U-net, the number of epochs was set to 40, as it contains both labeled and unlabeled data. Lastly, the hyperparameters in the combined loss of semisupervised U-net were set to  $\alpha = 1$  and  $\beta = 10$ .

### 4.1 Segmentation performance

For each trained architecture, the segmentation threshold was tuned on the validation set using both the topological score (optimizing topological consistency), and the segmentation loss (optimizing voxel-wise segmentation performance) for comparison. Optimal thresholds were applied to the test set, computing skeletons using the robust GEL skeletonization algo-

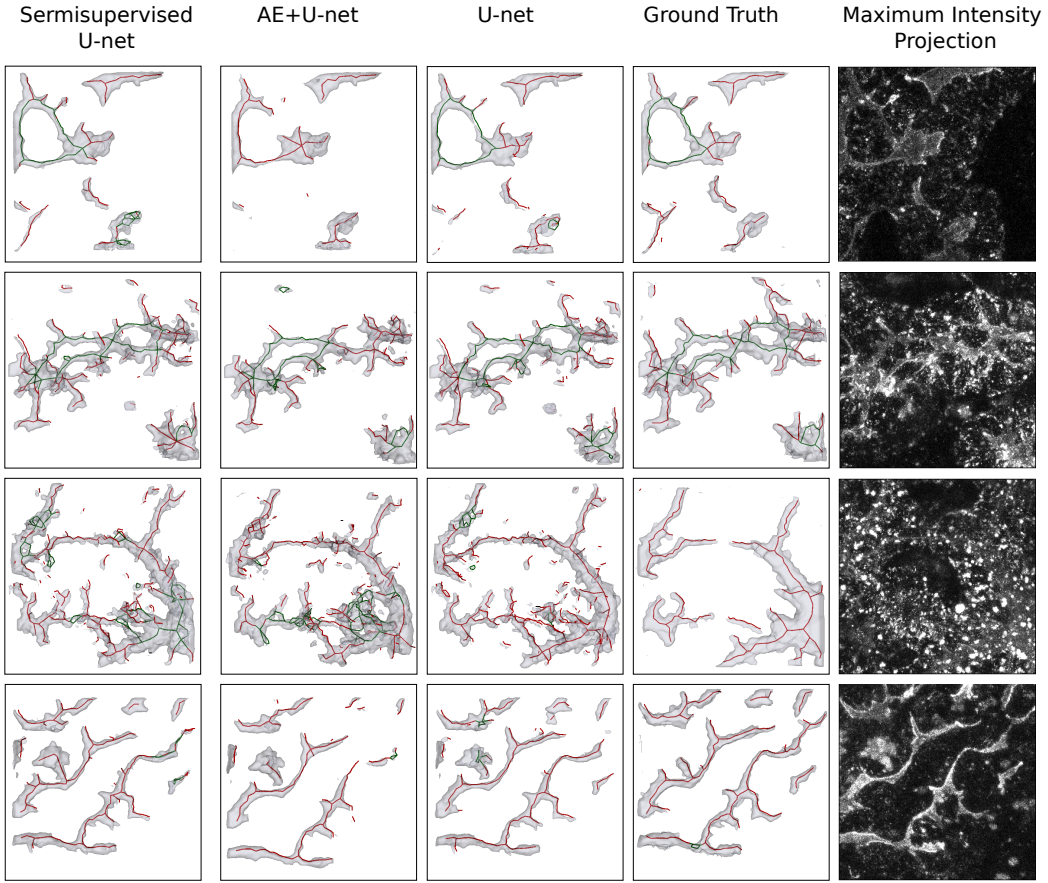


Figure 6: Segmentation results for 4 example test patches.

rithm Bærentzen and Rotenberg (2020); Bærentzen and et al. (2020). Skeleton components of size  $< 5$  nodes were ignored; the radius  $r = 10$  was used for node matching; and the thresholds  $t_{low} = 0.3$  and  $t_{high} = 0.7$  were used for the component and loop score matrices. Segmentations were validated using both the standard, voxel-level IoU, and the topological score derived in Sec. 2.1. Results are found in Table 1, where we report mean and standard deviation of patch-wise scores on the test set. Note that this standard deviation indicates variation in performance over different patches, not robustness over multiple training runs. Example segmentations for 4 example patches with the various models and their optimal thresholds (according to the topological score) are found in Fig. 6.

#### 4.2 Assessment of topological features

To assess our segmentation performance depends on the difficulty of the segmentation task, Fig. 7 shows topology score vs entropy (left) and distribution of topology-, component- and loop scores for patches of different segmentation difficulty. Both plots use the test set predictions of the semisupervised U-net.

## 5. Discussion and Conclusion

We tackled the challenging segmentation of pancreatic tubes from live-imaging microscopy. Our concerns were twofold: 1) Having a topologically accurate segmentation, and 2) learning features from plentiful unlabeled data to aid the segmentation. For the former, we contribute a topology score to quantify topological accuracy of segmentations. For the latter, we compared a fully-supervised U-net with two semi-supervised frameworks.

The enforcement of topology accuracy was limited to tuning the thresholding hyper-parameter, which expectedly improves segmentation topology over using the standard IoU (Table 1). We expect this can be further improved by modifying the topology score into a loss for training, but this is challenging both due to the computational burden of computing repeated skeletons, and the lack of smoothness when the skeleton varies over time.

Although the semisupervised U-net utilized the diversity of unlabeled data to improve segmentation, its predictions are not perfect. As shown in Fig. 7, our performance correlates negatively with segmentation entropy as well as segmentation difficulty as assessed by the trained expert. Thus, endowing the extracted tubular network with a notion of uncertainty could ensure safe interpretation.

While it may seem odd that AE+U-net is outperformed by a randomly initialized U-net, this was observed over multiple training runs, indicating that pretraining actually led to a worse initialization. Similar effects have also been observed in other applications Achille et al. (2018).

Our networks were 2D CNNs. While the 3D U-net Çiçek et al. (2016) utilizes useful spatial structure, it also has more parameters, which with our limited labeled data led to poorer performance than the 2D counterpart.

We have proposed a pipeline for segmenting tubular networks from noisy bioimages, utilizing a new topological scoring function for model selection and validation, as well as a semisupervised U-net for utilizing both labeled and unlabeled data. We illustrate how our performance correlates with data quality, and compared different semi-supervised settings with a fully-supervised model.

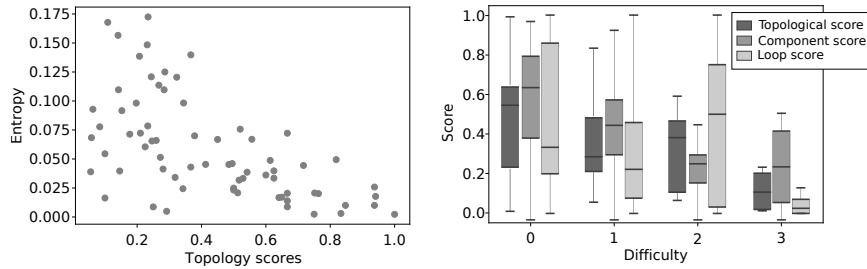


Figure 7: Left: Patch-wise topology score versus segmentation entropy. Right: Distribution of topology, component and loop scores divided over difficulty of manual labeling.

## References

Alessandro Achille, Matteo Rovere, and Stefano Soatto. Critical learning periods in deep networks. In *International Conference on Learning Representations*, 2018.

Andreas Bærentzen and Eva Rotenberg. Skeletonization via local separators. *arXiv preprint arXiv:2007.03483*, 2020.

Eric D Bankaitis, Matthew E Bechard, and Christopher VE Wright. Feedback control of growth, differentiation, and morphogenesis of pancreatic endocrine progenitors in an epithelial plexus niche. *Genes & development*, 29(20):2203–2216, 2015.

Andreas Bærentzen and et al. The GEL library. <http://www2.compute.dtu.dk/projects/GEL/>, 2020.

Özgün Çiçek, Ahmed Abdulkadir, Soeren S Lienkamp, Thomas Brox, and Olaf Ronneberger. 3d u-net: learning dense volumetric segmentation from sparse annotation. In *International conference on medical image computing and computer-assisted intervention*, pages 424–432. Springer, 2016.

Xiaoling Hu, Fuxin Li, Dimitris Samaras, and Chao Chen. Topology-preserving deep image segmentation. In Hanna M. Wallach, Hugo Larochelle, Alina Beygelzimer, Florence d’Alché-Buc, Emily B. Fox, and Roman Garnett, editors, *Advances in Neural Information Processing Systems 32: Annual Conference on Neural Information Processing Systems 2019, NeurIPS 2019, December 8-14, 2019, Vancouver, BC, Canada*, pages 5658–5669, 2019.

Gokul Kesavan, Fredrik Wolfhagen Sand, Thomas Uwe Greiner, Jenny Kristina Johansson, Sune Kobberup, Xunwei Wu, Cord Brakebusch, and Henrik Semb. Cdc42-mediated tubulogenesis controls cell specification. *Cell*, 139(4):791–801, 2009.

Rui Li, Muye Zhu, Junning Li, Michael S Bienkowski, Nicholas N Foster, Hanpeng Xu, Tyler Ard, Ian Bowman, Changle Zhou, Matthew B Veldman, et al. Precise segmentation of densely interweaving neuron clusters using g-cut. *Nature communications*, 10(1):1–12, 2019.

Fong Cheng Pan and Chris Wright. Pancreas organogenesis: from bud to plexus to gland. *Developmental Dynamics*, 240(3):530–565, 2011.

Yulei Qin, Mingjian Chen, Hao Zheng, Yun Gu, Mali Shen, Jie Yang, Xiaolin Huang, Yue-Min Zhu, and Guang-Zhong Yang. Airwaynet: A voxel-connectivity aware approach for accurate airway segmentation using convolutional neural networks. In *International Conference on Medical Image Computing and Computer-Assisted Intervention*, pages 212–220. Springer, 2019.

Alethia Villasenor, Diana C Chong, Mark Henkemeyer, and Ondine Cleaver. Epithelial dynamics of pancreatic branching morphogenesis. *Development*, 137(24):4295–4305, 2010.

Fan Wang, Huidong Liu, Dimitris Samaras, and Chao Chen. Topogan: A topology-aware generative adversarial network. In *European Conference on Computer Vision*, volume 2, 2020a.

Yan Wang, Xu Wei, Fengze Liu, Jieneng Chen, Yuyin Zhou, Wei Shen, Elliot K Fishman, and Alan L Yuille. Deep distance transform for tubular structure segmentation in ct scans. In *Proceedings of the IEEE/CVF Conference on Computer Vision and Pattern Recognition*, pages 3833–3842, 2020b.

Shihao Zhang, Huazhu Fu, Yuguang Yan, Yubing Zhang, Qingyao Wu, Ming Yang, Mingkui Tan, and Yanwu Xu. Attention guided network for retinal image segmentation. In *International Conference on Medical Image Computing and Computer-Assisted Intervention*, pages 797–805. Springer, 2019.